Stacking Order, Perfect Spin Polarization, and Giant Magnetoresistance in Zigzag Graphene/*h*-BN Heterobilayer Nanoribbons

Bing Luo,[1,2] Ruiling Gao,[1,2] Yin Wang,[1,2] Heng Gao,[1,2,3,4,5,*] Junjie Liu,[1,2,†] and Wei Ren[1,2,6,‡]

[1] *Department of Physics, International Center of Quantum and Molecular Structures, Shanghai University, Shanghai 200444, China*

[2] *Materials Genome Institute, State Key Laboratory of Advanced Special Steel and Shanghai Key Laboratory of High Temperature Superconductors, Shanghai University, Shanghai 200444, China*

[3] *Key Laboratory of Green Fabrication and Surface Technology of Advanced Metal Materials (Anhui University of Technology), Ministry of Education, Maanshan 243002, China*

[4] *State Key Laboratory of Surface Physics and Department of Physics, Fudan University, Shanghai 200433, China*

[5] *State Key Laboratory of Infrared Physics, Shanghai Institute of Technical Physics, Chinese Academy of Sciences, 200083, Shanghai, China*

[6] *Zhejiang Laboratory, Hangzhou 311100, China*

(Received 14 October 2022; revised 19 January 2023; accepted 24 January 2023; published 1 March 2023)

In a van der Waals heterostructure of two-dimensional materials, electronic properties are tunable by means of stacking orders. Here, we study the spin-dependent quantum transport in the bilayer of ferromagnetic zigzag-edged graphene/hexagonal-BN nanoribbons (ZGr-BNNRs) using density-functional theory combined with the Keldysh nonequilibrium Green's-function method. We reveal a strong odd-even effect of transport across the ZGr-BNNRs and a giant magnetoresistance value observed only in even-width ZGr-BNNRs. More interestingly, this value can be optimized by engineering stacking orders, yielding the perfect spin polarization efficiency of 100% and the magnetoresistance value of over 10^4 in even-width ZGr-BNNRs. Our results provide a route to design and fabricate high-performance spin filters and magnetic storage devices.

DOI: 10.1103/PhysRevApplied.19.034002

I. INTRODUCTION

Two-dimensional (2D) materials and the effects of their weak van der Waals (vdW) forces have attracted unprecedented attention. The weak vdW interaction between the thin atomic layers makes it possible to fabricate nanodevices whose performance can be controlled by the stacking orders between the layers [1–5], such as photolysis water [6,7] and ferroelectric tunnel junctions [8,9]. The stacking orders can break the inversion symmetry, giving rise to unique electrical and optoelectronic properties. For instance, in bilayer graphene, a slight variation in the twist angle of stacking may strongly modify the electronic properties, and a variety of phenomena have been observed, such as superconductivity [10,11], magnetism [12,13], topological Chern insulating states [14], and valley transport [15]. Likewise, in vdW bilayer hexagonal boron nitride (*h*-BN), stacking one monolayer of BN on another creates experimentally a moiré pattern consisting of AB and BA stacking order regions. The AB and BA stacking orders in bilayer BN exhibit opposite out-of-plane electric polarizations, which are evidenced by ferroelectricity in bilayer BN [16–19]. These findings highlight that the electronic properties are highly sensitive to stacking order. Additionally, *h*-BN is an appealing substrate material for graphene due to its excellent lattice matching with graphene and its flat surface [20–22]. The closely matched lattice constants produce a large moiré superlattice with near-zero mismatch [23,24].

Graphene coupled to *h*-BN can form a 2D vdW heterostructure whose physical properties are distinct from those of the individual layers [25–29]. For example, when graphene is aligned with *h*-BN, the band structure is significantly changed due to the hybridization of their bands. If a rotational angle is present between layers, a band gap of the graphene arises and a hexagonal moiré pattern of AB and BA stacking orders emerges, showing a modulated transition in the heterostructure [30]. Graphene devices on a *h*-BN substrate have carrier mobilities that are almost an order of magnitude larger than those in devices on a conventional SiO_2 substrate [31]. Several methods have been developed to fabricate the 2D vdW heterostructure with

*gaoheng@shu.edu.cn
†jj_liu@shu.edu.cn
‡renwei@shu.edu.cn

distinct stacking order by controlling rotation or sliding between layers, such as optical alignment of the crystal [32], alignment during thermal annealing [33], and artificially stamping flakes [18]. Meanwhile, there are several recent reports investigating the mechanical, electronic, and optical properties of the graphene/*h*-BN heterostructure [34–41]. Nevertheless, the relationship between the relative stacking orders between layers and ballistic transport properties remains largely unexplored. The ballistic transport properties are very important not only in fundamental science, but also in advanced nanoelectronics [42]. Thus, revealing the relationship can lead to promising applications in fabricating future electronic devices since the effects of stacking order endow the 2D materials with distinct characteristics and special properties that are impossible using only original 2D materials.

Here, we report quantum transport simulations of a 2D vdW heterostructure formed by graphene and *h*-BN with different stacking orders (AA, AB, and BA) by combining density-functional theory (DFT) with the Keldysh nonequilibrium Green's-function (NEGF) formalisms. Varying stacking order modifies not only the magnetoresistance values, but also the spin polarization efficiency. Our results reveal a giant magnetoresistance value of over 10^4 and the spin polarization efficiency of 100% in the even-width zigzag graphene/*h*-BN heterobilayer nanoribbons (ZGr-BNNRs), and these unique features can be understood from the transmission spectrum. Finally, we investigate the dependence of transmission spectrum on the bias voltage.

II. MODEL AND METHOD

The graphene/*h*-BN heterobilayer may have three different stacking orders (AA, AB, and BA) by considering interlayer sliding, and the geometry optimizations are shown in Fig. 1(a). These configurations are local energy minima, and range from the metastable AA stacking to stable AB stacking structure. Meanwhile, we calculate the binding energy of these structures to further prove the structural stability, indicating that the AB stacking structure is the most stable [43,44]. In AA, the C atoms in the top graphene layer fully overlap with the B and N atoms in the bottom boron nitride layer. In AB (BA) stacking, the

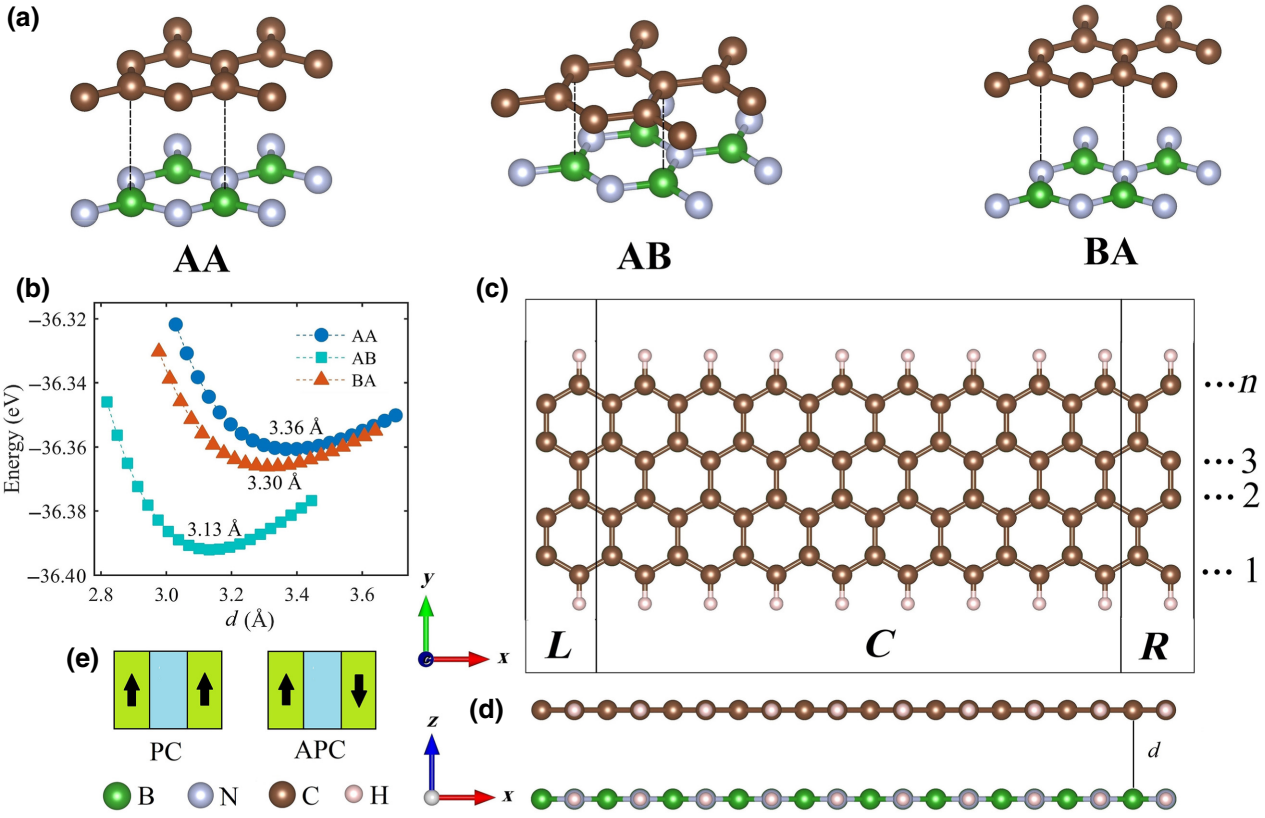

FIG. 1. (a) Illustration of the atomic arrangement for AA, AB, and BA stacking orders of graphene/*h*-BN heterobilayer. (b) Total energy in the primitive cell versus the interlayer distance. (c),(d) Top and side views of *n*-ZGr-BNNR two-probe device consisting of the left (*L*) and right (*R*) electrodes, and the central scattering region (*C*). The integer *n* is the width of the nanoribbons defined as the number of parallel zigzag chains. (e) Parallel configuration (PC) and antiparallel configuration (APC) for the magnetization directions of two electrodes.

B (N) atoms in the lower layer sit below the C atoms in the upper layer while the N (B) atoms in the lower layer are below the empty site at the center of the hexagon in the upper layer, as shown in Fig. 1(a). Figure 1(b) shows the energy in the primitive cell (containing C_2BN atoms) as a function of the interlayer distance (d) between graphene and boron nitride layers, where AB stacking exhibits a typical minimum. The interlayer distances of three configurations (AA, AB, and BA) are 3.36 Å, 3.13 Å, and 3.30 Å, respectively, which are in excellent agreement with previous reports [26]. To study electronic transport properties of the graphene/h-BN heterobilayer, we construct a two-probe device composed of n ZGr-BNNRs (width $n = 3$, 4, 5, 6) with hydrogen-passivated edges, as schematically shown in Figs. 1(c) and 1(d). The semi-infinite left and right electrodes (L and R) are attached to the central scattering region (C). We choose eight unit cells as the length of the central scattering region, which is long enough to screen out the coupling between the left and right electrodes. A large vacuum distance of about 25 Å is employed to eliminate the interaction of the periodic image.

The geometric optimizations are carried out with the Vienna *ab initio* simulation package (VASP) [45]. In the VASP calculations, a cutoff energy of 500 eV is adopted for the plane-wave basis, and all structures are fully relaxed until the forces are smaller than 0.02 eV $Å^{-1}$ on each atom. The electronic structure and transport properties are implemented in the first-principles NanoAcademic device calculator (NANODCAL) package based on DFT combined with NEGF formalisms [46]. In the NEGF DFT numerical calculations, the generalized gradient approximation in the Perdew-Burke-Ernzerhof form is employed for the exchange-correlation functional. A real-space cutoff energy of 100 hartree and a double-zeta polarization linear-combination-of-atomic orbital basis are used for all atoms. A $100 \times 1 \times 1$ Monkhorst-Pack k-point mesh is used. We focus on the spin-dependent ballistic transport properties, and the spin-dependent electric current through the central scattering region can be obtained from the Landauer formula [47],

$$I_\sigma(V_b) = \frac{e}{h} \int T_\sigma(E, V_b)[f_l(E - \mu_l) - f_r(E - \mu_r)]dE \quad (1)$$

where the $\sigma = \uparrow$ (spin up) or $\sigma = \downarrow$ (spin down), and the corresponding spin polarization efficiency (η) is defined as $\eta \equiv |(I_\uparrow - I_\downarrow)/(I_\uparrow + I_\downarrow)|$, $\mu_{l,r}$ are the electrochemical potentials of the left and right electrodes, $f_{l,r}$ are the Fermi-Dirac distribution functions of the left and right electrodes, e is the charge of the electron, and h is Planck's constant. The energy region of the transmission spectrum that contributes to the electric current is referred to as the bias window. In the range of a finite bias voltage V_b, the spin-dependent transmission spectrum $T_\sigma(E, V_b)$ is evaluated by [48]

$$T_\sigma(E, V_b) = \mathrm{Tr}[\Gamma_l(E, V_b)G^R(E, V_b)\Gamma_r(E, V_b)G^A(E, V_b)], \quad (2)$$

where $\Gamma_{l(r)}$ describes the coupling between the left (right) electrode and the central scattering region, namely the linewidth function. $G^{R(A)}$ is the retarded (advanced) Green's function, and E is the electron energy.

In each structure of the ZGr-BNNR device, the magnetization directions of the two electrodes can be aligned in a parallel configuration (PC) or antiparallel configuration (APC). The magnetoresistance (MR) of the two-probe system is then calculated by [49]

$$\mathrm{MR} = \frac{I_{\mathrm{PC}} - I_{\mathrm{APC}}}{I_{\mathrm{APC}}}, \quad (3)$$

where I_{PC} and I_{APC} are the total electric current ($I_{\mathrm{total}} = I_\uparrow + I_\downarrow$) in the PC and APC of the electrodes.

III. RESULTS AND DISCUSSION

In each electrode of the ZGr-BNNR device, there are two spin states at the edges corresponding to the ferromagnetic (FM) state and antiferromagnetic state. The FM state could easily be the ground state with the help of an external magnetic field and the magnetic order can be stable even at room temperature [50]. Thus, all systems in this work adopt the FM state. In Fig. 2, we display the APC spin-polarized currents and total electric currents as functions of bias voltage for 5- and 6-ZGr-BNNRs. In Supplemental Material Fig. S1 [51], for PC, we find that the spin-polarized currents are equal and the spin polarization efficiency is zero ($I_{\mathrm{up}} = I_{\mathrm{down}}$, $\eta = 0$), and the total electric currents remain the same for all systems, regardless of the stacking type.

From the spin-polarized currents and total electric currents in Fig. 2, we can obtain the magnetoresistance and spin polarization efficiency η, which respectively measure the magnetic detection sensitivity of the system and the magnitude of spin polarization during electron transport, as shown in Fig. 3. For APC 5-ZGr-BNNR, the increasing gradient of total electric current decreases as the bias voltage increases in Figs. 2(a)–2(c), leading to a significantly increasing MR (Fig. 3). The spin-polarized currents $I_{\mathrm{up}} \approx I_{\mathrm{down}}$ are quite close in BA stacking, which causes a small η as can be seen from the inset of Fig. 3(c). As for APC 6-ZGr-BNNR, we find that the spin-polarized currents are drastically different in magnitude as $I_{\mathrm{up}} \gg I_{\mathrm{down}}$ for both AA and BA stackings, while $I_{\mathrm{up}}\ I_{\mathrm{down}}$ for AB stacking. This suggests that spin-up (spin-down) electrons in the AA and BA stackings (AB stacking) easily go through the system under nonzero bias, while the transport of spin-down (spin-up) electrons is almost blocked.

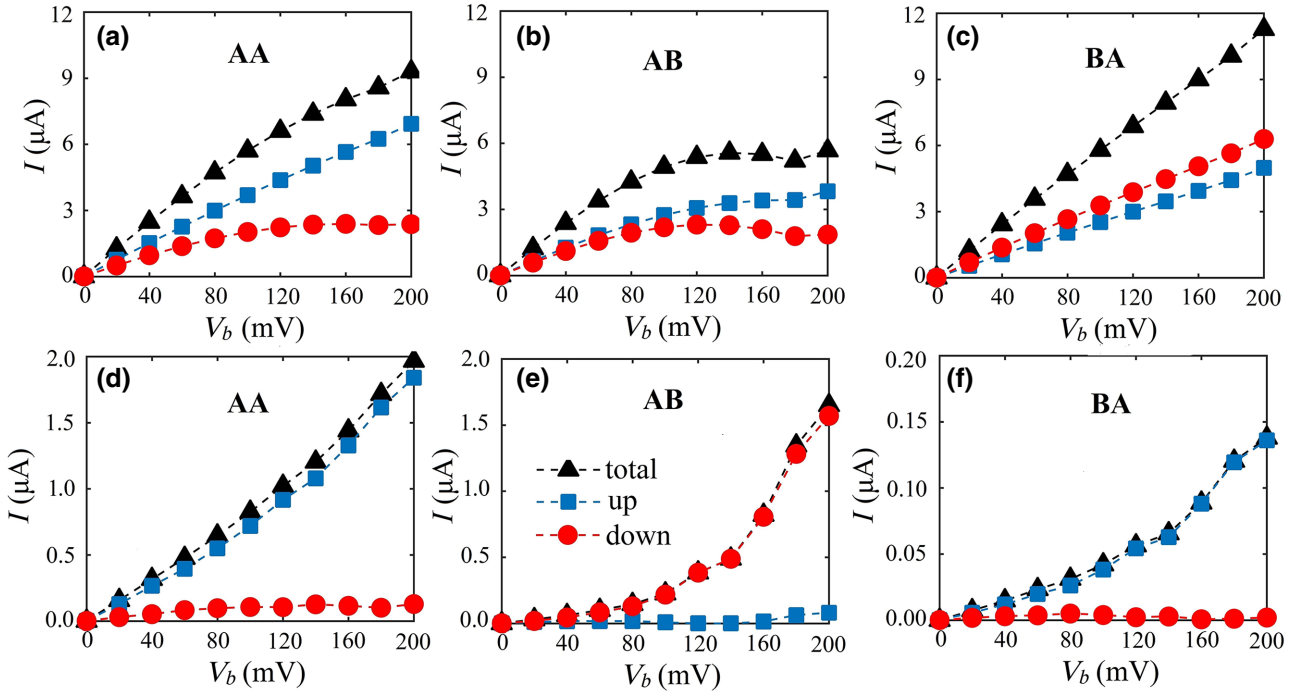

FIG. 2. Spin-polarized currents and total electric currents as function of bias voltages in the AA, AB, and BA stackings of APC, respectively, (a)–(c) for 5-ZGr-BNNR and (d)–(f) for 6-ZGr-BNNR.

These interesting findings indicate that even-width 6-ZGr-BNNR can act as a spin filter. The 3- and 4-ZGr-BNNRs results are analyzed similarly, as shown in Supplemental Material Figs. S2 and S3 [51]. We highlight the emergence of strong odd-even characteristics of the MR and η by comparing odd- and even-width ZGr-BNNRs. The MR of

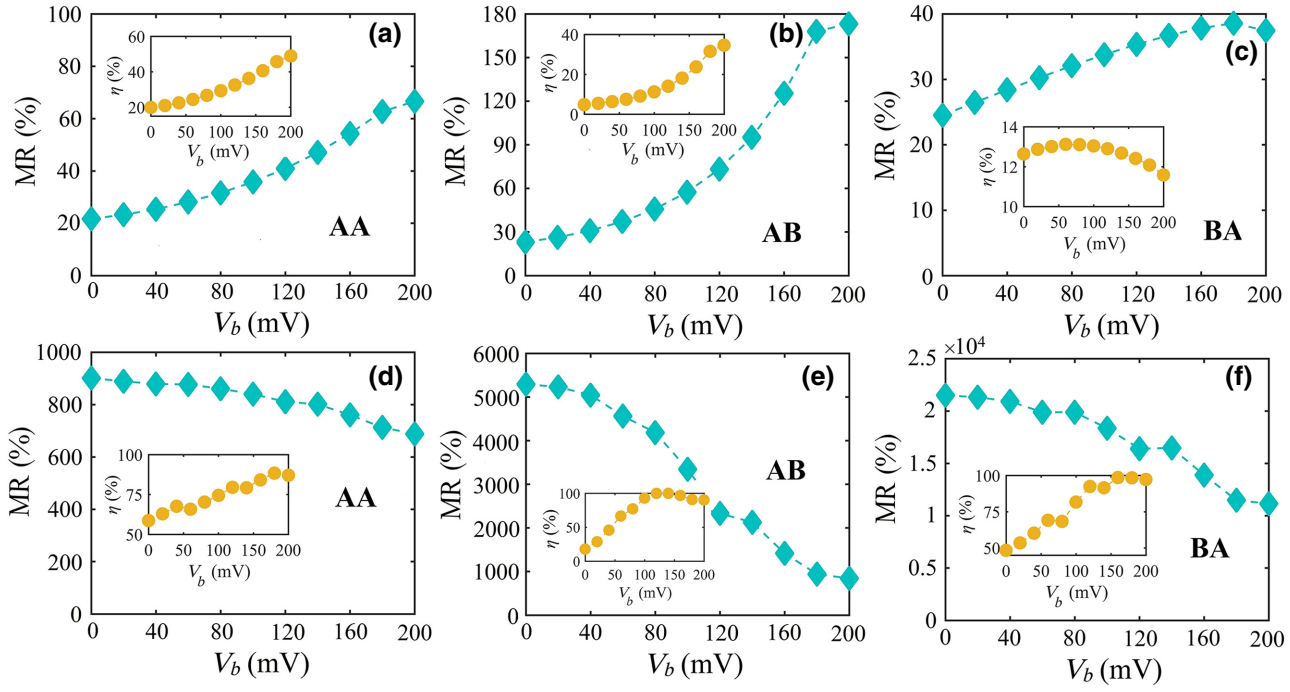

FIG. 3. MR and η (inset) versus bias voltages for the AA, AB, and BA stackings. Upper panels (a)–(c) are for 5-ZGr-BNNR, and lower panels (d)–(f) are for 6-ZGr-BNNR. Note that 6-ZGr-BNNR has significantly larger MR and η than 5-ZGr-BNNR.

even-width 6-ZGr-BNNR is at least 1 order of magnitude larger than that of odd-width 5-ZGr-BNNR, and a distinct increasing trend of η is revealed with the increase of bias voltage. More interestingly, the MR can be optimized by interlayer sliding in even-width 6-ZGr-BNNR, and the maximum MR reaches 2×10^4 and η realizes 100% for BA stacking. In order to understand the origin of the giant MR observed in even-width ZGr-BNNR, we plot the local density of states (LDOS) distribution of the central scattering region as a function of the energy and position x for AA, AB, and BA stackings, as shown in Figs. S4 and S5 in the Supplemental Material [51]. The AA stacking possesses a larger LDOS distribution near the Fermi energy, compared with AB and BA stackings, in which fewer electronic states contribute to the transport. Thus, the AA stacking features higher transmission probability, but the resulting giant MR occurs in AB and BA stackings.

Furthermore, the interesting odd-even characteristics can be understood not only from the transmission spectra of the central scattering region, but also from the electronic band structures of the two electrodes for the system at zero bias. In Fig. 4, we show transmission coefficients through the central scattering region and the electronic band structures in the two electrodes for 5- and 6-ZGr-BNNRs in the PC and APC. The energy bands of both spin edge states tend to flatten near the X point in the PC for 5- and 6-ZGr-BNNRs, as shown in Figs. 4(a) and 4(c), which may result in two sharp spin transmission coefficient peaks away from the Fermi level. Moreover, the transmission coefficients within the bias window are essentially 1 for both spin states; the spin-polarized currents ($I_{\rm up} = I_{\rm down}$) and the total electric currents remain the same in the PC for all systems (Fig. S1 in the Supplemental Material [51]). Meanwhile, for the APC, we observe that the transmission coefficients of n-ZGr-BNNR with odd ($n = 5$) and even ($n = 6$) widths have distinct behaviors, in accordance with the odd-even effect shown in Fig. 3. For odd-width 5-ZGr-BNNR, the transmission coefficient has a plateau near the Fermi level, while for even-width 6-ZGr-BNNR, the transmission coefficient is almost zero near the Fermi level. As a consequence, the giant MR appears in the even-width 6-ZGr-BNNR [Figs. 3(d)–3(f)]. These results are similar to those for silicene [52] and α-graphyne [53] nanoribbons in the literature.

We remark that n-ZGr-BNNRs with odd and even widths have similar electronic band structures near the Fermi level, hence the difference in the transmission coefficients near the Fermi level in the APC does not originate from the difference in the electronic band structures, but results from the electron wave function mismatch. For odd-width 5-ZGr-BNNR, the wave functions of π and π^* subbands in the two electrodes do not have any specific

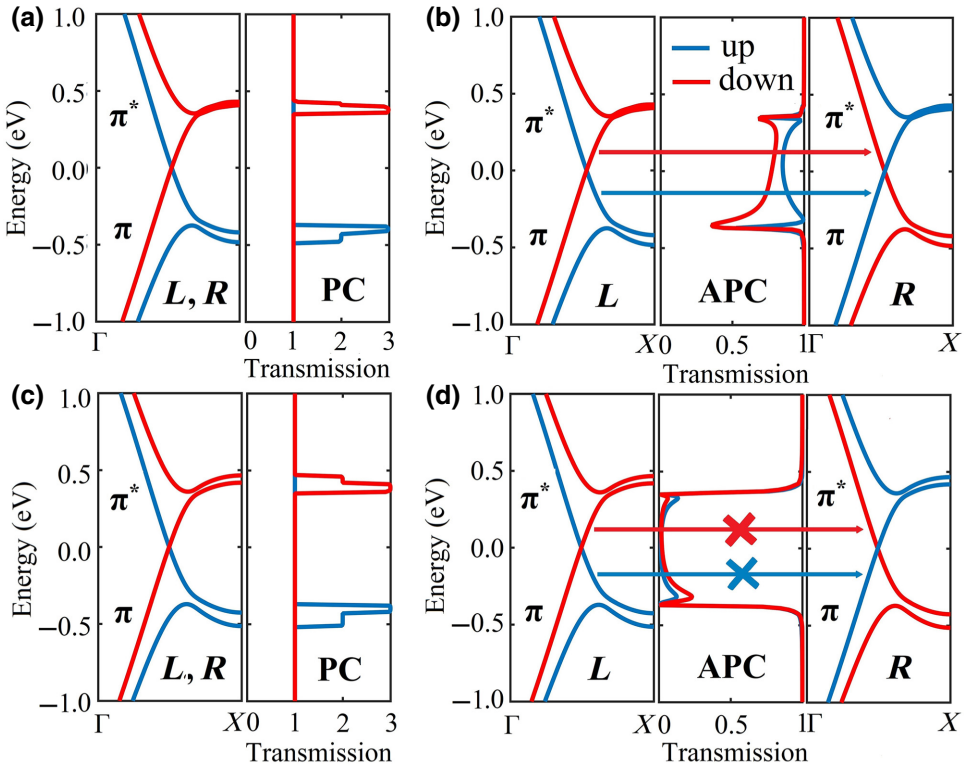

FIG. 4. The electronic band structures in both electrodes and the transmission coefficients through the central scattering region under zero bias voltage in the PC and APC of AB stacking for (a),(b) 5-ZGr-BNNR and (c),(d) 6-ZGr-BNNR. In (d) we indicate the forbidden transport processes near the Fermi level due to the orthogonality of the wave functions of the left and right electrodes.

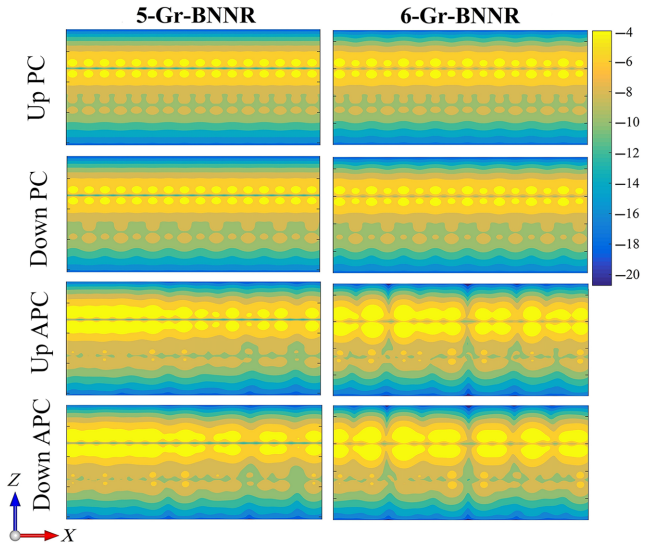

FIG. 5. The scattering states at the Fermi level incident under zero bias of AB stacking in the PC and APC for 5- and 6-ZGr-BNNRs. The color bar represents the amplitude of the scattering states. All the figures share the same color bar.

symmetry. There is no symmetry-imposed selective rule to hinder electronic transport from spin up (spin down) electrons in the π^* (π) state of the left electrode to the π (π^*) state of the right electrode. However, the case becomes different for even-width 6-ZGr-BNNR, as the wave functions of π (π^*) subbands are antisymmetric (symmetric) about the central axis of the system [54]. The wave functions of π subbands in one electrode are orthogonal to those of π^* subbands in the other electrode. This implies that the electron transmission from π subbands of the left electrode to π^* subbands of the right electrode is blocked. This mismatch of the wave functions in the two electrodes results in a sharp drop in transmission coefficient near the Fermi level. These results explain why the giant MR can be observed in even-width 6-ZGr-BNNR but not in odd-width 5-ZGr-BNNR.

In order to gain a more intuitive understanding of the transport properties, we now show the scattering states at the Fermi level incident under zero bias. Figure 5 presents the AB stacking for 5- and 6-ZGr-BNNRs as examples, and the scattering states of other stackings can be analyzed similarly (see Supplemental Material Figs. S6–S9 [51]). For the PC, regardless of width parity, the scattering states are consistent through the central scattering region, and the wave functions extend all the way along the entire nanoribbon to contribute to the transport. For the APC, the scattering states get weaker and weaker from the left to right electrode, leading to a reduction in transmission coefficient at the Fermi level.

In addition to this transport property analysis at zero bias voltage of transmission coefficients and the scattering states, we now look at the transmission coefficients $T_\sigma(E,V_b)$ as a function of a finite bias V_b ranging from 0 to 200 mV. The spin-polarized currents and total electric currents in Fig. 2 are obtained by integrating over the bias window $-V_b/2 \le E \le V_b/2$. Figure 6 depicts $T_\sigma(E,V_b)$ versus electron energy in the AB stacking of the APC for 5-

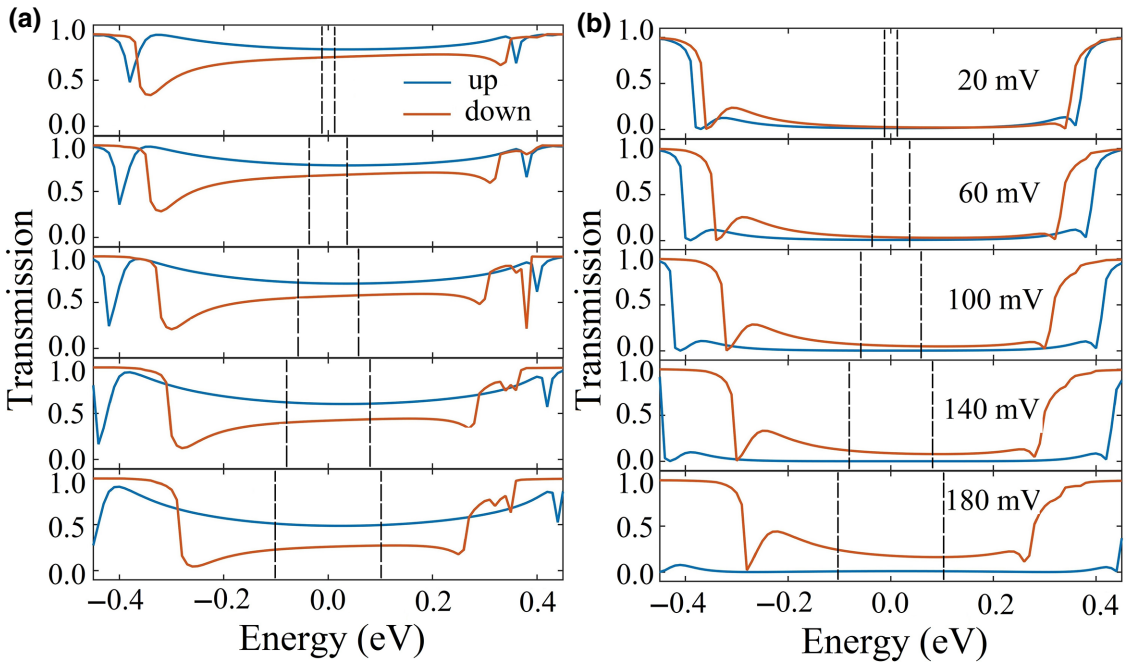

FIG. 6. Transmission coefficients as function of electron energy under different bias voltages in AB stacking of the APC for (a) 5- and (b) 6-ZGr-BNNRs. The vertical dashed lines represent the bias window, and the Fermi level is set at zero energy.

and 6-ZGr-BNNRs, and other configurations are illustrated in Supplemental Material Figs. S10 and S11 [51]. Several distinct features are worth mentioning: (1) For the PC, the transmission coefficients near the Fermi level maintain substantial and stable values within the bias window, hence explaining the finding in the inset of Fig. S1 in the Supplemental Material [51] that the spin-polarized currents and total electric currents in the PC increase linearly with the increase of the bias and remain the same for all systems, respectively. In addition, the spin-up transmission coefficient peaks around $E = -0.4$ eV and the spin-down transmission coefficient has a broad peak near $E = 0.4$ eV. These obvious transmission coefficient peaks are diminished when increasing the bias voltage. (2) For the APC, it is observed that the spin-up channel has a larger transmission than the spin-down channel within the bias window in AB stacking for odd-width 5-ZGr-BNNR [Fig. 6(a)], and the opposite is true for the even-width 6-ZGr-BNNR [Fig. 6(b)], explaining the result of $I_{up} > I_{down}$ ($I_{up} < I_{down}$) in the AB stacking for odd-width 5-ZGr-BNNR (even-width 6-ZGr-BNNR) [Figs. 2(b) and 2(e)]. (3) Both spin-up and spin-down transmission coefficients within the bias window in even-width 6-ZGr-BNNR are much smaller than those in odd-width 5-ZGr-BNNR, explaining the giant MR in even-width 6-ZGr-BNNR compared with that in odd-width 5-ZGr-BNNR. Similar transport properties can also be observed in the odd-width 3-ZGr-BNNR and even-width 4-ZGr-BNNR (see Supplemental Material Figs. S12 and S13 [51]). These results show a strong odd-even effect, which is in good agreement with the previous reported results [52–54].

IV. SUMMARY

In summary, we investigate the quantum transport properties of the *n*-ZGr-BNNR heterobilayer by combining the DFT with Keldysh NEGF methods. The nanoribbons of four different widths ($n = 3$, 4, 5, 6) are constructed, each system including three different stacking orders (AA, AB, and BA), and the width-dependent odd-even effect for the ZGr-BNNR heterobilayer is found. Spin polarization efficiency up to 100% and giant magnetoresistance with a ratio of over 10^4 can be observed in even-width ZGr-BNNRs. Such distinctive behaviors are rooted in the symmetry of the wave function near the Fermi level. In even-width ZGr-BNNR, the wave functions of the π subbands in one electrode are orthogonal to those of the π^* subbands in the other electrode, resulting in an increase of the magnetoresistance by several orders of magnitudes compared with the odd-width counterpart. Interestingly, the magnetoresistance for even-width ZGr-BNNR can be significantly improved by varying stacking order. For 6-ZGr-BNNR, the perfect spin polarization efficiency and giant magnetoresistance are observed in both AB and BA stackings, and maintain stable large values over a broad range of external bias voltages. These unique features can be understood by the analyses of the transmission coefficients. Our results suggest that the ZGr-BNNR heterobilayer may have potential applications for designing highly efficient spin filters and magnetic storage devices.

ACKNOWLEDGMENTS

This work was supported by the National Natural Science Foundation of China (12074241, 52130204, 11929401), the Science and Technology Commission of Shanghai Municipality (22XD1400900, 20501130600, 21JC1402600, 22YF1413300), High Performance Computing Center, Shanghai University, Key Research Project of Zhejiang Lab (No. 2021PE0AC02), Key Research and Development Program of Shaanxi Province (No. 2021GXLH-Z-065), and the open projects of Key Laboratory of Green Fabrication and Surface Technology of Advanced Metal Materials (Anhui University of Technology), Ministry of Education (No. GFST2022KF08), State Key Laboratory of Surface Physics (Fudan University) (No. KF2022_10), and State Key Laboratory of Infrared Physics, Shanghai Institute of Technical Physics, Chinese Academy of Sciences (No. SITP-NLIST-YB-2022-08).

[1] C. J. Kim, L. Brown, M. W. Graham, R. Hovden, R. W. Havener, P. L. McEuen, D. A. Muller, and J. Park, Stacking order dependent second harmonic generation and topological defects in *h*-BN bilayers, Nano Lett. **13**, 5660 (2013).

[2] G. Constantinescu, A. Kuc, and T. Heine, Stacking in Bulk and Bilayer Hexagonal Boron Nitride, Phys. Rev. Lett. **111**, 036104 (2013).

[3] S. M. Gilbert, T. Pham, M. Dogan, S. Oh, B. Shevitski, G. Schumm, S. Liu, P. Ercius, S. Aloni, M. L. Cohen, and A. Zettl, Alternative stacking sequences in hexagonal boron nitride, 2D Mater. **6**, 021006 (2019).

[4] M. T. Greenaway, E. E. Vdovin, A. Mishchenko, O. Makarovsky, A. Patanè, J. R. Wallbank, Y. Cao, A. V. Kretinin, M. J. Zhu, S. V. Morozov, *et al.*, Resonant tunnelling between the chiral Landau states of twisted graphene lattices, Nat. Phys. **11**, 1057 (2015).

[5] A. Mishchenko, *et al.*, Twist-controlled resonant tunnelling in graphene/boron nitride/graphene heterostructures, Nat. Nanotechnol. **9**, 808 (2014).

[6] W. Zhang, H. Wang, C. H. Shi, S. Y. Liu, S. Y. Chang, and C. He, Tunable electronic and optical properties of a planar hydrogenated AsSi hybrid nanosheet: A potential wide water-splitting photocatalyst, J. Phys. Chem. C **123**, 14999 (2019).

[7] C. He, F. Han, and W. Zhang, The InSe/g-CN van der Waals hybrid heterojunction as a photocatalyst for water splitting driven by visible light, Chin. Chem. Lett. **33**, 404 (2022).

[8] Y. Chen, Z. Tang, M. Dai, X. Luo, and Y. Zheng, Giant magnetoresistance and tunneling electroresistance in multiferroic tunnel junctions with 2D ferroelectrics, Nanoscale **14**, 8849 (2022).

[9] Z. Yan, Z. Li, Y. Han, Z. Qiao, and X. Xu, Giant tunneling magnetoresistance and electroresistance in α-In_2Se_3-based van der Waals multiferroic tunnel junctions, Phys. Rev. B **105**, 075423 (2022).

[10] Y. Cao, V. Fatemi, S. Fang, K. Watanabe, T. Taniguchi, E. Kaxiras, and P. J. Herrero, Unconventional superconductivity in magic-angle graphene superlattices, Nature **556**, 43 (2018).

[11] M. Yankowitz, S. Chen, H. Polshyn, Y. Zhang, K. Watanabe, T. Taniguchi, D. Graf, A. F. Young, and C. R. Dean, Tuning superconductivity in twisted bilayer graphene, Science **363**, 1059 (2019).

[12] A. L. Sharpe, E. J. Fox, A. W. Barnard, J. Finney, K. Watanabe, T. Taniguchi, M. A. Kastner, and D. G. Gordon, Emergent ferromagnetism near three-quarters filling in twisted bilayer graphene, Science **365**, 605 (2019).

[13] L. A. Gonzalez-Arraga, J. L. Lado, F. Guinea, and P. San-Jose, Electrically Controllable Magnetism in Twisted Bilayer Graphene, Phys. Rev. Lett. **119**, 107201 (2017).

[14] E. M. Spanton, A. A. Zibrov, H. Zhou, T. Taniguchi, K. Watanabe, M. P. Zaletel, and A. F. Young, Observation of fractional Chern insulators in a van der Waals heterostructure, Science **360**, 62 (2018).

[15] L. Ju, Z. Shi, N. Nair, Y. Lv, C. Jin, J. Velasco, Jr, C. Ojeda-Aristizabal, H. A. Bechtel, M. C. Martin, A. Zettl, *et al.*, Topological valley transport at bilayer graphene domain walls, Nature **520**, 650 (2015).

[16] E. Y. Tsymbal, Two-dimensional ferroelectricity by design, Science **372**, 1389 (2021).

[17] K. Yasuda, X. Wang, K. Watanabe, T. Taniguchi, and P. Jarillo-Herrero, Stacking-engineered ferroelectricity in bilayer boron nitride, Science **372**, 1458 (2021).

[18] M. Vizner Stern, Y. Waschitz, W. Cao, I. Nevo, K. Watanabe, T. Taniguchi, E. Sela, M. Urbakh, O. Hod, and M. B. Shalom, Interfacial ferroelectricity by van der Waals sliding, Science **372**, 1462 (2021).

[19] L. Li and M. Wu, Binary compound bilayer and multilayer with vertical polarizations: Two-dimensional ferroelectrics, multiferroics, and nanogenerators, ACS Nano **11**, 6382 (2017).

[20] G. Giovannetti, P. A. Khomyakov, G. Brocks, P. J. Kelly, and J. van den Brink, Substrate-induced band gap in graphene on hexagonal boron nitride: *Ab initio* density functional calculations, Phys. Rev. B **76**, 073103 (2007).

[21] R. Decker, Y. Wang, V. W. Brar, W. Regan, H. Z. Tsai, Q. Wu, W. Gannett, A. Zettl, and M. F. Crommie, Local electronic properties of graphene on a BN substrate via scanning tunneling microscopy, Nano Lett. **11**, 2291 (2011).

[22] Y. Yang, Y. Peng, M. F. Saleem, Z. Chen, and W. Sun, Hexagonal boron nitride on III–V compounds: A review of the synthesis and applications, Materials **15**, 4396 (2022).

[23] C. R. Woods, *et al.*, Commensurate–incommensurate transition in graphene on hexagonal boron nitride, Nat. Phys. **10**, 451 (2014).

[24] R. Ribeiro-Palau, C. Zhang, K. Watanabe, T. Taniguchi, J. Hone, and C. R. Dean, Twistable electronics with dynamically rotatable heterostructures, Science **361**, 690 (2018).

[25] M. Yankowitz, J. Xue, D. Cormode, J. D. Sanchez-Yamagishi, K. Watanabe, T. Taniguchi, P. Jarillo-Herrero, P. Jacquod, and B. J. LeRoy, Emergence of superlattice Dirac points in graphene on hexagonal boron nitride, Nat. Phys. **8**, 382 (2012).

[26] W. Hu and J. Yang, Two-dimensional van der Waals heterojunctions for functional materials and devices, J. Mater. Chem. C **5**, 12289 (2017).

[27] W. Zhang, J. Zhang, C. He, and T. Li, Constructing Janus SnSSe and graphene heterostructures as promising anode materials for Li-ion batteries, Int. J. Energy Res. **46**, 267 (2021).

[28] Y. Wu, C. He, and W. Zhang, Novel design strategy of high activity electrocatalysts toward nitrogen reduction reaction via boron-transition-metal hybrid double-atom catalysts, ACS Appl. Mater. Interfaces **13**, 47520 (2021).

[29] C. He, Y. Liang, and W. Zhang, Design of novel transition-metal-doped C_6N_2 with high-efficiency polysulfide anchoring and catalytic performances toward application in lithium-sulfur batteries, ACS Appl. Mater. Interfaces **14**, 29120 (2022).

[30] N. R. Finney, M. Yankowitz, L. Muraleetharan, K. Watanabe, T. Taniguchi, C. R. Dean, and J. Hone, Tunable crystal symmetry in graphene-boron nitride heterostructures with coexisting moire superlattices, Nat. Nanotechnol. **14**, 1029 (2019).

[31] C. R. Dean, A. F. Young, I. Meric, C. Lee, L. Wang, S. Sorgenfrei, K. Watanabe, T. Taniguchi, P. Kim, K. L. Shepard, and J. Hone, Boron nitride substrates for high-quality graphene electronics, Nat. Nanotechnol. **5**, 722 (2010).

[32] C. R. Dean, L. Wang, P. Maher, C. Forsythe, F. Ghahari, Y. Gao, J. Katoch, M. Ishigami, P. Moon, M. Koshino, *et al.*, Hofstadter's butterfly and the fractal quantum Hall effect in moiré superlattices, Nature **497**, 598 (2013).

[33] D. Wang, *et al.*, Thermally Induced Graphene Rotation on Hexagonal Boron Nitride, Phys. Rev. Lett. **116**, 126101 (2016).

[34] X. Zhong, Y. K. Yap, R. Pandey, and S. P. Karna, First-principles study of strain-induced modulation of energy gaps of graphene/BN and BN bilayers, Phys. Rev. B **83**, 193406 (2011).

[35] C. Yelgel and G. P. Srivastava, Ab initio studies of electronic and optical properties of graphene and graphene–BN interface, Appl. Surf. Sci. **258**, 8338 (2012).

[36] T. Cao, X. Zheng, L. Huang, P. Gong, and Z. Zeng, Hydrogen-coverage-dependent stark effect in bilayer graphene and graphene/BN nanofilms, J. Phys. Chem. C **118**, 10472 (2014).

[37] G. Casiano-Jiménez, C. Ortega-López, J. A. Rodríguez-Martínez, M. G. Moreno-Armenta, and M. J. Espitia-Rico, Electronic structure of graphene on the hexagonal boron nitride surface: A density functional theory study, Coatings **12**, 237 (2022).

[38] L. Patra, G. Mallick, G. Sachdeva, C. Shock, and R. Pandey, Orientation-dependent mechanical response of graphene/BN hybrid nanostructures, Nanotechnology **32**, 235707 (2021).

[39] J. Wang, L. Ge, A. Deng, H. Qiu, H. Li, Y. Zhu, and M. Bo, Atomic bonding and electrical characteristics of two-dimensional graphene/boron nitride van der Waals heterostructures with manufacturing defects via binding energy and bond-charge model, Chem. Phys. Lett. **794**, 139474 (2022).

[40] Q. Cao, L. Xu, and J. Zhang, Spintronic phase transition of graphene/BN/graphene van de Waals heterostructures, Results Phys. **35**, 105344 (2022).

[41] B. Lyu, *et al.*, Catalytic growth of ultralong graphene nanoribbons on insulating substrates, Adv. Mater. **34**, 2200956 (2022).

[42] J. Baringhaus, M. Ruan, F. Edler, A. Tejeda, M. Sicot, A. Brahimi, A. Li, Z. Jiang, E. H. Conrad, C. Berger, *et al.*, Exceptional ballistic transport in epitaxial graphene nanoribbons, Nature **506**, 349 (2014).

[43] W. X. Zhang, Y. Yin, and C. He, Spontaneous enhanced visible-light-driven photocatalytic water splitting on novel type-II GaSe/CN and Ga_2SSe/CN vdW heterostructures, J. Phys. Chem. Lett. **12**, 5064 (2021).

[44] Y. B. Wu, C. He, and W. X. Zhang, "Capture-backdonation-recapture" mechanism for promoting N_2 reduction by heteronuclear metal-free double-atom catalysts, J. Am. Chem. Soc. **144**, 9344 (2022).

[45] G. Kresse and J. Furthmüller, Efficiency of ab-initio total energy calculations for metals and semiconductors using a plane-wave basis set, Comp. Mater. Sci. **6**, 15 (1996).

[46] J. Taylor, H. Guo, and J. Wang, *Ab initio* modeling of quantum transport properties of molecular electronic devices, Phys. Rev. B **63**, 245407 (2001).

[47] M. Sun, X. Wang, and W. Mi, Large magnetoresistance in Fe_3O_4/4, 4′-bipyridine/Fe_3O_4 organic magnetic tunnel junctions, J. Phys. Chem. C **122**, 3115 (2018).

[48] X. Yang, F. Tan, Y. Dong, H. Yu, and Y. Liu, Transition metal-containing molecular devices: controllable single-spin negative differential thermoelectric resistance effects under gate voltages, Phys. Chem. Chem. Phys. **21**, 5243 (2019).

[49] G. D. Zhao, L. M. Li, Y. Wang, A. Stroppa, J. H. Zhang, and W. Ren, Modifying spin current filtering and magnetoresistance in a molecular spintronic device, RSC Adv. **8**, 41587 (2018).

[50] G. Z. Magda, X. Jin, I. Hagymási, P. Vancsó, Z. Osváth, P. Nemes-Incze, C. Hwang, L. Biró, and L. Tapasztó, Room-temperature magnetic order on zigzag edges of narrow graphene nanoribbons, Nature **514**, 608 (2014).

[51] See Supplemental Material at http://link.aps.org/supplemental/10.1103/PhysRevApplied.19.034002 for LDOS distribution of the central scattering region as a function of the energy and position x, the scattering states, and the transmission coefficients as a function of a finite bias for AA, AB, and BA stackings.

[52] A. B. Chen, X. F. Wang, P. Vasilopoulos, M. X. Zhai, and Y. S. Liu, Spin-dependent ballistic transport properties and electronic structures of pristine and edge-doped zigzag silicene nanoribbons: Large magnetoresistance, Phys. Chem. Chem. Phys. **16**, 5113 (2014).

[53] M. X. Zhai, X. F. Wang, P. Vasilopoulos, Y. S. Liu, Y. J. Dong, L. Zhou, Y. J. Jiang, and W. L. You, Giant magnetoresistance and spin Seebeck coefficient in zigzag alpha-graphyne nanoribbons, Nanoscale **6**, 11121 (2014).

[54] J. Zeng, K. Q. Chen, J. He, X. J. Zhang, and C. Q. Sun, Edge hydrogenation-induced spin-filtering and rectifying behaviors in the graphene nanoribbon heterojunctions, J. Phys. Chem. C **115**, 25072 (2011).